Article

# Allomelanin: A Biopolymer of Intrinsic Microporosity

Naneki C. McCallum, Florencia A. Son, Tristan D. Clemons, Steven J. Weigand,
Karthikeyan Gnanasekaran, Claudia Battistella, Brooke E. Barnes, Hashanthi Abeyratne-Perera,
Zofia E. Siwicka, Christopher J. Forman, Xuhao Zhou, Martin H. Moore, Daniel A. Savin,
Samuel I. Stupp, Zheng Wang, Gary J. Vora, Brandy J. Johnson, Omar K. Farha,
and Nathan C. Gianneschi*

Cite This: *J. Am. Chem. Soc.* 2021, 143, 4005−4016

Read Online

ACCESS | Metrics & More | Article Recommendations | Supporting Information

**ABSTRACT:** Melanin is a ubiquitous natural pigment found in a diverse array of organisms. Allomelanin is a class of nitrogen-free melanin often found in fungi. Herein, we find artificial allomelanin analogues exhibit high intrinsic microporosity and describe an approach for further increasing and tuning that porosity. Notably, the synthetic method involves an oxidative polymerization of 1,8-DHN in water, negating the need for multiple complex templating steps and avoiding expensive or complex chemical precursors. The well-defined morphologies of these nanomaterials were elucidated by a combination of electron microscopy and scattering methods, yielding to high-resolution 3D reconstruction based on small-angle X-ray scattering (SAXS) results. Synthetic allomelanin nano-



particles exhibit high BET areas, up to 860 m$^2$/g, and are capable of ammonia capture up to 17.0 mmol/g at 1 bar. In addition, these nanomaterials can adsorb nerve agent simulants in solution and as a coating on fabrics with high breathability where they prevent breakthrough. We also confirmed that naturally derived fungal melanin can adsorb nerve gas simulants in solution efficiently despite lower porosity than synthetic analogues. Our approach inspires further analysis of yet to be discovered biological materials of this class where melanins with intrinsic microporosity may be linked to evolutionary advantages in relevant organisms and may in turn inspire the design of new high surface area materials.
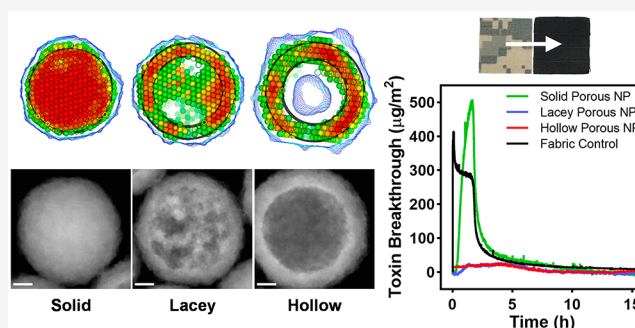
## INTRODUCTION

Melanin is a versatile pigment found in almost every type of organism on earth.[1] It serves a variety of known functions in nature such as radiation protection,[2] metal chelation,[3,4] thermoregulation,[5] and structural coloration.[6] Melanins have also been shown to exhibit more exotic properties such as toxin adsorption in melanic sea snakes[7] and butter clams.[8] For the past decade, the interest in synthetic melanin, specifically human eumelanin, has grown significantly, with the vast majority of studies centered almost entirely around the oxidative polymerization of dopamine to form polydopamine (PDA).[9−16] This inspired us to explore the richer chemistry of melanin beyond PDA for access to new types of function. Specifically, here, we focus on allomelanin-derived 1,8-dihydroxynaphthalene (1,8-DHN), a monomer that is utilized in nature by fungi. Allomelanins, the nitrogen-free family of melanins, are present in nature not as a pure substance but as a complex material associated with polysaccharides and proteins, although this composition has yet to be quantified.[17,18] Therefore, an artificial mimic provides an approach toward pure materials for understanding the unique properties of allomelanin itself. Synthetic allomelanin mimics have only

recently been synthesized by using chemoenzymatic and chemical synthetic methods to oligomerize and polymerize 1,8-DHN.[19−21] The latter affords discrete, spherical particles with low dispersity and with excellent radical scavenging properties.[21] With a straightforward, high-yielding synthesis in hand, we reasoned, based on the chemical structure of the oligomers and polymers generated from 1,8-DHN, that the materials could likely exhibit intrinsic microporosity. This would also suggest that this could be the case for allomelanin produced by organisms. Indeed, structural analogues in synthetic systems include polymers of intrinsic microporosity (PIMs) which have previously utilized naphthalene diol-type comonomers to afford materials with surface areas of up to 440−540 m$^2$/g.[22] For PIMs,[23,24,18] the voids created by inefficient packing of the resulting macromolecules give rise to
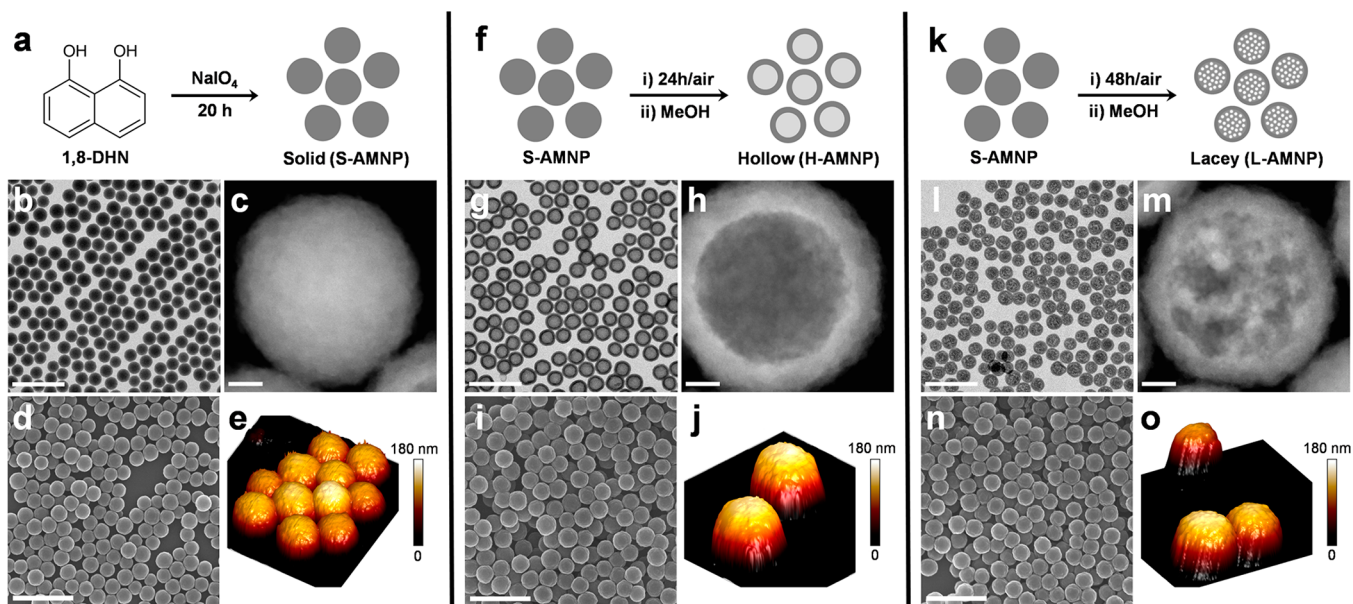
**Figure 1.** Schematic of allomelanin nanoparticle (AMNP) synthesis, with characterization by bright-field scanning transmission electron microscopy (BF-STEM), high-angle annular dark-field STEM (HAADF-STEM), scanning electron microscopy (SEM), and atomic force microscopy (AFM). (a−e) 1,8-DHN is oxidized by using $NaIO_4$ to form self-assembled, "solid" spherical structures (S-AMNP) which can be partially dissolved in MeOH at discrete time points to form "hollow" (H-AMNP, f−j) or "lacey" (L-AMNP, k−o) nanostructures. (a) S-AMNP synthetic scheme. (b) BF-STEM. (c) HAADF-STEM. (d) SEM. (e) AFM. (f) H-AMNP synthetic scheme. (g) BF-STEM. (h) HAADF-STEM. (i) SEM. (j) AFM. (k) L-AMNP synthetic scheme. (l) BF-STEM. (m) HAADF-STEM. (n) SEM. (o) AFM. All SEM and BF-STEM scale bars 500 nm, and all HAADF-STEM scale bars are 20 nm.

microporosity, and this property could very well provide organisms generating such materials in the form of melanin pigments an evolutionary advantage.

Herein, we report a biomimicry approach to develop synthetic porous materials. We show that amorphous, tunable, high-porosity allomelanin nanoparticles can be readily synthesized in a facile manner with minimal reagents. The resulting materials can be used for gas and toxin adsorption, inspiring the intriguing possibility that organisms use 1,8-DHN to generate porous functional materials.

## RESULTS AND DISCUSSION

**Preparation of Spherical Allomelanin Nanoparticles (S-AMNP).** Artificial allomelanin was synthesized by oxidative polymerization using 1,8-dihydroxynaphthalene (1,8-DHN) as a precursor (Figure 1). Synthetic allomelanin initially forms as a mixture of mainly dimers and low molecular weight oligomers as oxidative polymerization from 1,8-DHN proceeds over 20 h (Figure S1).[20,21,25] This mixture of dimers, trimers, and higher order oligomers assemble to form spherical ("solid") particles (S-AMNP) spontaneously in solution (Figure 1a−e and Figure S2). Bright-field, scanning transmission electron microscopy (BF-STEM) (Figure 1b) reveals uniform, spherical structures. High-angle annular dark-field STEM (HAADF-STEM) was also performed to view the particles at higher resolution (Figure 1c). Particle surfaces are visible by scanning electron microscopy (SEM) (Figure 1d) and more clearly visible by atomic force microscopy (AFM) (Figure 1e). Over time we observed a visible darkening of the particles in aqueous solution, from gray to black, correlated to polymerization and cross-linking. UV−vis absorbance was monitored from 1 to 15 days after synthesis of the S-AMNPs, revealing a broadening of the peak at ∼250 nm and a shift to longer wavelengths, indicative of expansion of the conjugated

system. This is coupled with an increase in the visible region as particles further oxidize and become darker in color, consistent with previous observations of these types of systems (Figure S3).[26] Solvent stability was assessed in preparation for porosity measurements which necessitate the use of ethanol, or a solvent with low surface tension that is miscible with liquid $CO_2$, for storage prior to supercritical activation. We observed that the initially formed allomelanin nanoparticles partially dissolved in ethanol but became stable in solution after aging, polymerizing and darkening. Because of the initially observed instability, a solvent screen was performed by using several organic solvents to determine the effects on the particles (Figure S4). Methanol (MeOH) was discovered to have profound effects on the particle morphology in the first 3 days after synthesis, resulting in well-defined structures (Figures S5−S7). Chemical changes in the dimer content were also observed up to 2 weeks following synthesis (Figure S8).

**Preparation of Hollow Allomelanin Nanoparticles (H-AMNP).** As observed by STEM, the aging process for generating AMNPs corresponds with an increase in solvent compatibility. The observations also resulted in the serendipitous discovery that particles aged for 24 h could be etched to well-defined, hollow AMNPs (H-AMNP) (Figure 1f−j and Figure S6). STEM micrographs show uniform, hollow structures (Figure 1g) that are more clearly visible by HAADF-STEM, wherein there appears a clear distinction between the hollow core and the shell (Figure 1h). H-AMNPs were ultramicrotomed to 80 nm sections, and imaged via STEM, revealing a hollow core (Figure S9). The particles persist as stable suspensions when stored in water at room temperature for at least 18 months (Figure S10) and at a wide range of pH values, as determined by a zeta-potential titration from pH 0 to 12 (Figure S11).
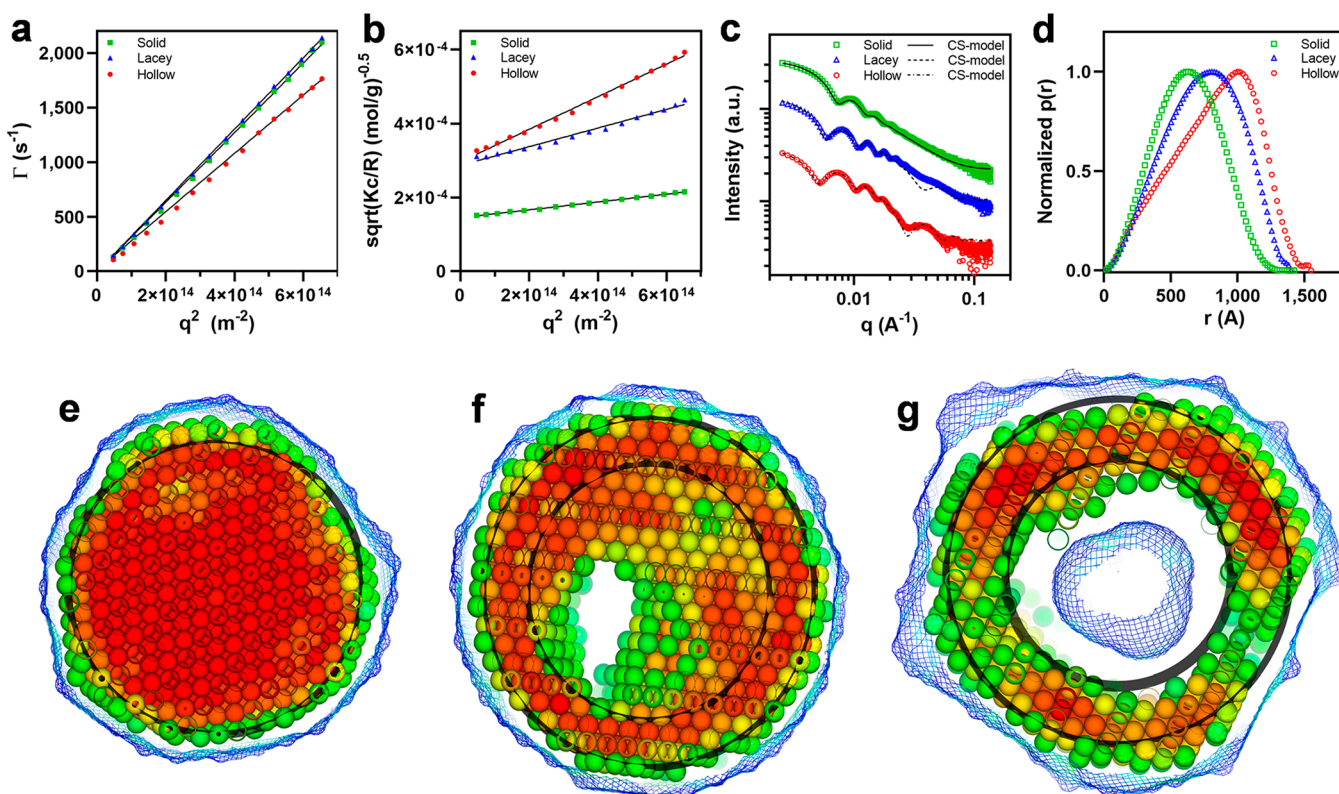
**Figure 2.** Scattering analysis of solid (S-AMNP), hollow (H-AMNP), and lacey (L-AMNP) nanoparticles by using dynamic light scattering (DLS), static light scattering (SLS), and small-angle X-ray scattering (SAXS). (a) DLS plot of the average decay rate of the autocorrelation function ($\Gamma$) vs the square of the scalar magnitude of the scattering vector ($q^2$), showing the particles have high uniformity. (b) SLS plot for deriving the radius of gyration ($R_g$). (c) SAXS patterns for AMNPs and scattering patterns from spherical core−shell (CS) geometric modeling. (d) Normalized pair distance distribution functions ($p(r)$). (e−g) Representative cross sections (each 400 Å thick) of the average dummy atom modeling (DAMs) for S-, L-, and H-AMNPS, respectively. Color coding represents the normalized bead probability from 0 (blue) to 1 (red); only beads with occupancy >1/3 are shown. Blue mesh represents the surface of all the beads with occupancy >0.1, accessible to an imaginary 180 Å solvent molecule. The cross-sectioned black spheres are for comparison only and have the same radii as the nanoparticle dimensions determined by core−shell modeling of the experimental SAXS.[27]

**Preparation of Lacey Allomelanin Nanoparticles (L-AMNP).** With a method for routinely generating hollow, spherical H-AMNPs, we reasoned that further aging followed by etching with methanol would lead to a higher surface area particle, with more internal structure (Figure 1k−o and Figure S6). STEM micrographs show structures that are an intermediate between S- and H-AMNP, with material density in the center having a lacey appearance (Figure 1l). HAADF-STEM imaging reveals the core of the particle with small voids throughout (Figure 1m). We hypothesized that this was due to the redeposition process of leached oligomers back onto the particle surface where they are further oxidized as a polymeric shell (*vide infra*).

**Bulk Solution Morphology Characterization by Light and X-ray Scattering.** We next conducted light and X-ray scattering studies to ascertain the dispersity, morphology, and fine structure of the materials in bulk solution (Figure 2). First, AMNPs were analyzed by using multiangle dynamic light scattering (DLS) and static light scattering (SLS) in water. The effective diffusion coefficient ($D_{eff}$) was primarily invariant with $q^2$ for all samples, with this angular independence indicative of their low dispersity (Figure S12). Hydrodynamic diameters ($D_h$) of 154 nm (S-AMNP), 150 nm (L-AMNP), and 184 nm (H-AMNP) were determined by DLS (Figure 2a and Figure S13, eqs S1 and S2). The effective radius of gyration ($R_g$) was obtained via multiangle SLS (Figure 2b and eq S3) with the

parameter $\rho = R_g/R_h$ giving an estimate of the compositional distribution of the particles. AMNP $R_g$ values were determined to be 66 nm (S-AMNP), 73 nm (L-AMNP), and 94 nm (H-AMNP), with $\rho$ values of 0.86 (S-AMNP), 0.97 (L-AMNP), and 1.02 (H-AMNP) corresponding to solid spheres in the case of S-AMNP, with an increasing distribution of mass toward the shell, commensurate with that observed by STEM, for L- and H-AMNP, respectively.

Small-angle X-ray scattering (SAXS) was performed on AMNPs that were synthesized 1 month prior to measurement and compared to that of a "fresh" S-AMNP sample synthesized 48 h prior (Figure S14 and eq S4). The 1D SAXS patterns from each nanoparticle sample were fit with a spherical core−shell model by using a Gaussian distribution (Figure 2c). In the case of S-AMNP, to minimize contributions of the shell thickness, the shell was fixed to 0.001 Å, and the X-ray scattering length density of the shell constrained to match that of solvent ($H_2O$, $9.42 \times 10^{10}$ $cm^{-2}$). Through these constraints, the core−shell model mathematically reduces to be very similar to that of a solid spheroid. To further confirm this, no appreciable difference was observed in the quality of fit or the modeled radius for the solid melanin nanoparticles modeled with a simple spheroid or the constrained core−shell model as shown in Figure S15. This allowed for the direct comparison of parameters across the three melanin nano-particles by using the same geometrical model. We also

analyzed the pair distance distribution function ($p(r)$) with $D_{max}$ (the maximum diameter of the particle) determined (Figure 2d and Figure S16). S-AMNPs follow a normal distribution as expected for solid spherical nanoparticles of smooth surface and uniform density. H-AMNPs display skewed distribution in $p(r)$ to higher $r$ values as expected for a hollow interior and significant shell density. Finally, L-AMNPs demonstrate peak broadening and skewness suggesting inhomogeneity within the core. The $D_{max}$ for S-AMNPs (142.4 nm), L-AMNPs (140.0 nm), and H-AMNPs (155.0 nm) is in strong agreement with values calculated from core–shell modeling of X-ray scattering and those observed also by light scattering experiments. Modeling demonstrates H-AMNP have the largest overall particle radius of 71 nm and greatest shell thickness of 23 nm. In comparison, S-AMNP exhibited the smallest total radius of 61 nm and L-AMNP a total radius of 69 nm with a shell contribution of 16 nm (Tables S1 and S2). 3D reconstructions (Figure 2e–g) reveal structures in good agreement with STEM and light scattering data.

The SAXS analysis software suite ATSAS was used to further investigate the melanin nanoparticle structures by using an *ab initio* dummy atom modeling (DAM) approach. In this approach, each atom/bead represents an occupied volume element of either particle phase or solvent phase.[27] These beads are initially randomly assigned phases after which point the calculated scattering of the modeled particle is refined against the experimental scattering data by randomly switching the phase of the beads, while gradually reducing the probability of accepting those changes that do not improve the fit (Figures S17 and 18, Table S3). Renderings of the averaged DAMs for each nanoparticle, with the bead occupancy probability color coded from 0 to 1 (blue to red, respectively), support the differences observed between melanin nanoparticles (Figure 2e–g). Hence, red represents a high probability that the bead position is occupied across the averaged DAM through to blue representing a low probability for this bead position. DAM for S-AMNP matches the core–shell modeled sphere of radius 61 nm and has a uniform high probability of bead occupancy throughout the nanoparticle (Figure 2e). The average DAM for L-AMNP exhibits a core–shell structure which is in strong agreement with core–shell fitting with low probabilities for bead occupancies throughout the core of the nanoparticle, suggesting a randomly dispersed lacey internal structure (Figure 2f). Finally, the average DAM of H-AMNP has a shell of significantly high bead occupancy probability, with a hollow core in good agreement with core–shell fitting analysis (Figure 2g). The average DAM of fresh S-AMNPs produced a model with similar characteristics to aged S-AMNPs (Figure S19). A more comprehensive 3D representation can be viewed in the accompanying videos (Videos S1–S4).

**Mechanism of Formation of AMNPs.** Scattering experiments and initial STEM imaging led us to the hypothesis that at early time points after synthesis S-AMNPs retain a "molten core" of loosely associated small oligomers that can be dissolved in organic solvent. These small molecules can then leach out of the micropores into solution, where they eventually redeposit back onto the particle surface over time as the etching solution remains in contact with the particles. Hollow particles are formed by etching at an earlier time point; therefore, the core is less oxidized and more susceptible to dissolution, whereas 24 h later, the etching process leads to lacey particles due to increasingly oxidized particles which are less susceptible to dissolution by MeOH. To further probe the

mechanistic details of formation of the various morphologies of AMNPs and to test our hypothesis of the formation process, high-angle dark-field scanning electron microscopy (HAADF-STEM) images were obtained and analyzed for size and material density distribution throughout the particles (Figure 3). For these studies, and due to the distinct morphologies, a
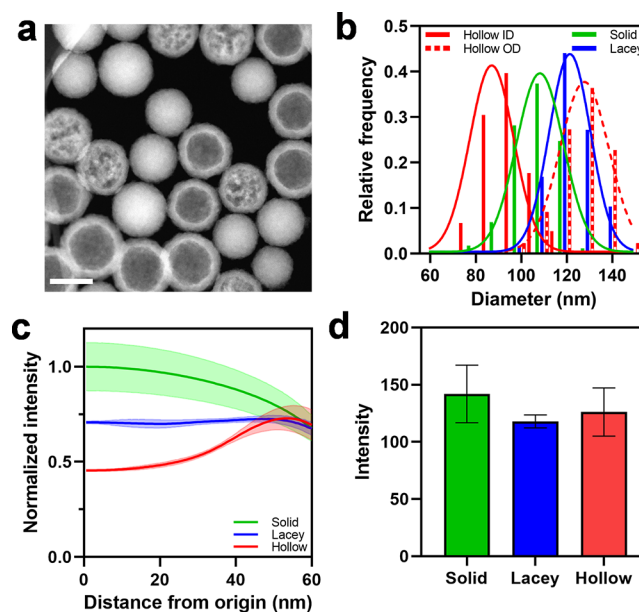


**Figure 3.** HAADF-STEM analysis of AMNPs. (a) HAADF-STEM micrograph of 1:1:1 solid:lacey:hollow AMNP mixture used for size and intensity analyses. (b) Frequency distributions for S- and L-AMNP diameters as well as the inner (ID) and outer (OD) diameters of H-AMNP. (c) Normalized intensity as a function of the distance from the center of a single AMNP. The lightly colored area around each curve is the standard deviation of the measurements of at least four AMNP particles. (d) Total intensity normalized by area of AMNP.

mixture of 1:1:1 solid:lacey:hollow AMNP was analyzed on a single lacey carbon TEM grid to provide a uniform background signal for the intensity measurements (Figure 3a). The S- and L-AMNP diameters were measured as well as the H-AMNP inner diameter (ID) and outer diameter (OD). The frequency distribution shows that H-AMNP OD increases in relation to the amount of material dissolved from the inside of the particle. H-AMNPs lose the most material from inside the particle and therefore have the largest OD. The H-AMNP ID is smaller than the OD of the S-AMNP, indicating that some of the original S-AMNP shell remains as material is lost from the inner volume (Figure 3b).

To quantify the relative difference in volume of the material within the particle, we measured the radial intensity profile from the center to the periphery of individual nanoparticles (Figure 3c and Figure S20). Indeed, the relative volume of material follows expected trends, with S-AMNPs the most densely packed in the core and H-AMNPs the least. For all three particles, the outer "shells" converged to the same relative volume of material.

To confirm whether there was conservation of material across each AMNP independent of morphology, we determined the overall total intensity from HAADF-STEM images (Figure 3d). Here, irrespective of morphology, total intensity is very similar, indicating negligible loss of material.
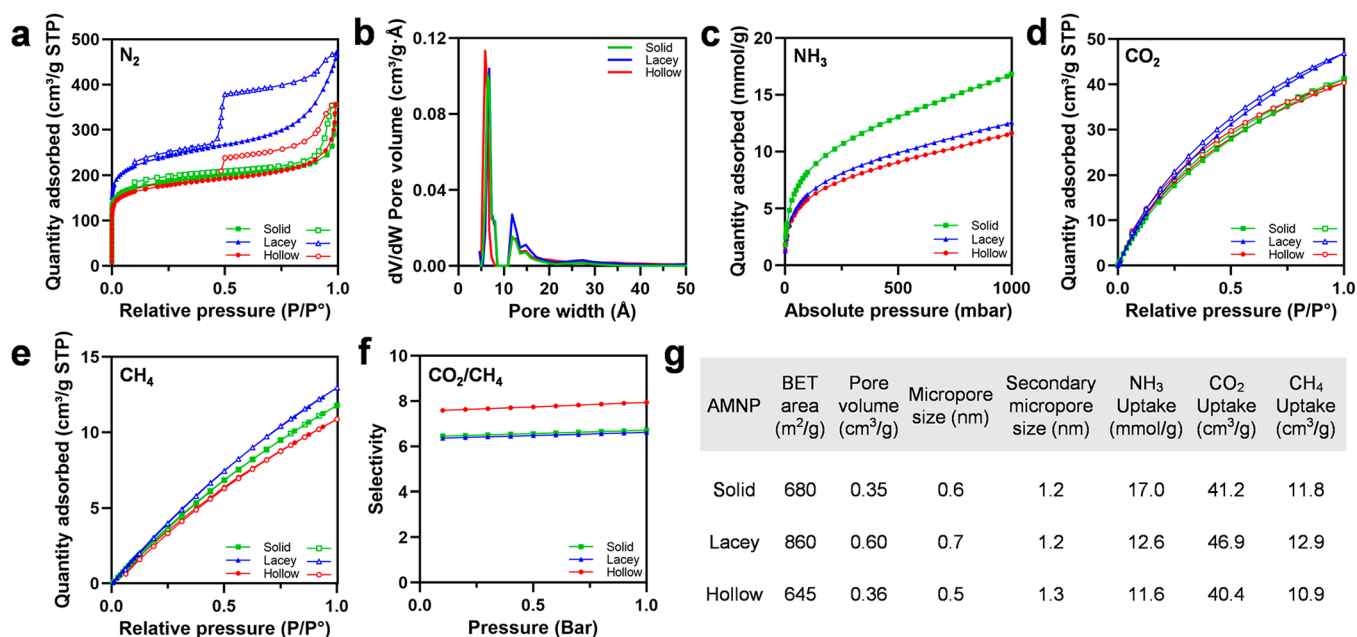
**Figure 4.** Sorption measurements for solid (S-AMNP), lacey (L-AMNP), and hollow (H-AMNP) nanoparticles and pore size calculations. For sorption measurements, closed markers represent adsorption and open markers represent desorption. (a) Nitrogen isotherms. (b) Pore volume measurements. (c) $NH_3$ uptake. (d) $CO_2$ uptake. (e) $CH_4$ uptake. (f) IAST calculation for a mixture of mole fractions 0.05 $CO_2$ and 0.95 $CH_4$. (g) Summarized sorption measurements and pore sizes for AMNPs.

This is consistent with the mechanism of formation of L- and H-AMNPs leaching oligomers from their cores and redepositing them onto the particle surface, growing the OD of the particle by using core material (Figure S21). This is also consistent with the STEM time series that shows that particles etched at 24 or 48 h but not incubated over several days with the etching solution have shells that collapse when dried onto a TEM grid (Figures S5 and S6).

**Sorption Measurements.** To assess the porosity of AMNPs, nitrogen physisorption measurements were performed at 77 K (Figure 4). The particles were first activated by using supercritical $CO_2$ (Figure S22). Nitrogen isotherms revealed Brunauer−Emmett−Teller (BET) areas of 680 $m^2/g$ for S-AMNPs, 645 $m^2/g$ for H-AMNPs, and 860 $m^2/g$ for L-AMNPs (Figure 4a). DFT calculations showed two major pores around 6 and 12 Å for all AMNPs, although L-AMNP pore volume (0.60 $cm^3/g$) was significantly higher than for S-AMNPs (0.35 $cm^3/g$) or H-AMNPs (0.36 $cm^3/g$) (Figure 4b), which is consistent with the larger voids seen via HAADF-STEM. Based on our pore-size distribution analysis, there were no distinct mesopores present in L-AMNPs. Although from the STEM data we can see mesoporous voids, based on the surface characterization conducted from the $N_2$ isotherms, we believe that these mesopores are highly irregular in size and present only in low concentrations. Beyond 2 nm, the $dV/dW$ pore volume is close to zero, which points to the low quantity of these mesopores in our materials (Figure S23). We hypothesized that due to the −OH groups present on the surface of the porous AMNPs, these materials would be promising for ammonia capture and/or storage.[28] Therefore, we obtained ammonia adsorption isotherms at 298 K (Figure 4c). The samples were degassed and placed under vacuum ($P/P_0 \sim 10^{-6}-10^{-7}$) prior to measurements. The ammonia isotherms showed steep and high uptake at lower pressures arising from strong interactions between the AMNPs and $NH_3$, which indicates that these materials would be promising for air

filtration applications. At 1 bar, $NH_3$ uptakes for the S-, L-, and H-AMNPs were 17.0, 12.6, and 11.6 mmol/g, respectively. We hypothesize that S-AMNP had the highest $NH_3$ uptake due to an increase of functional group density per gram of material. Despite it having a lower surface area, this higher density could have facilitated $NH_3$ adsorption. These porous materials have comparable performance in total uptake at 1 bar to metal−organic frameworks[28−31] and porous organic polymers.[32,33]

To probe the efficacy of AMNPs for gas storage and separation applications, $CO_2$ and $CH_4$ isotherms were collected at 298 K (Figure 4d,e). The total $CO_2$ uptake is similar to that seen in microporous organic polymers[34] (S-AMNP = 41.2 $cm^3/g$, L-AMNP = 46.9 $cm^3/g$, and H-AMNP = 40.4 $cm^3/g$) and is higher than observed for $CH_4$ (S-AMNP = 11.8 $cm^3/g$, L-AMNP = 12.9 $cm^3/g$, and H-AMNP = 10.9 $cm^3/g$). To determine whether AMNPs could be utilized for carbon dioxide separation from natural gas consisting predominantly of methane, we quantified their selectivity through the application of ideal adsorbed solution theory (IAST)[35] on the pure gas isotherms fitted using the BET model (Figures S24−S26). Using gas phase mole fractions of 0.05 for $CO_2$ and 0.95 for $CH_4$, which is a typical composition for natural gas purification, IAST calculations were performed at 1 bar (consistent with collected measurements) and predicted selectivities ranging from 6 to 8 were obtained (Figure 4f). These selectivities indicated that $CO_2$ was preferentially adsorbed over $CH_4$. The stronger interactions between AMNPs and $CO_2$ were attributed to the presence of hydroxyl moieties present on the surface.[36,37] Despite L-AMNPs having the highest storage capacity, the selectivity (6.5) was comparable to that of the S-AMNP. H-AMNP had the highest selectivity of around 7.5, perhaps arising to the higher density of functional groups present on the surface per unit volume, as indicated by the lower pore volume of 0.36 $cm^3/g$. Beyond preferential adsorption due to surface functionalization, the microporous nature of these particles

may have aided in increased uptake of $CO_2$, which has a smaller kinetic diameter of 3.3 Å compared to that of $CH_4$ (3.8 Å). AMNP selectivities were on the order of those of ZIF-8[38] and glucose-derived porous carbon spheres[39] and close to those of mixed-ligand metal−organic frameworks.[40] Therefore, we predict that these particles could be useful for $CO_2$ separation from natural gas. The total uptake for $CO_2$ and $CH_4$ followed surface area trends, indicating that the total loadings of these molecules were less impacted by intermolecular interactions than for $NH_3$. The combined sorption measurements are compared in Figure 4g.

**Toxin Adsorption in Solution.** Given the high porosity of AMNPs and success with ammonia capture, we next tested whether they could serve as toxin remediation agents upon exposure to diazinon and paraoxon, which are common pesticides and are used as analogues for structurally similar chemical warfare agents.[41,42] A known mass of AMNP (10, 20, or 40 $\mu$g $\pm$ 1 $\mu$g) was incubated with either diazinon or paraoxon for 2 h, after which the solution was filtered by using a 0.2 $\mu$m PTFE syringe filter. Analysis of the target remaining in the sample was performed by HPLC, and the resulting data were fit by using the Langmuir isotherm to generate the saturation loading for the materials in grams/gram and an affinity coefficient (1/M) (Figure 5 and eq S5).
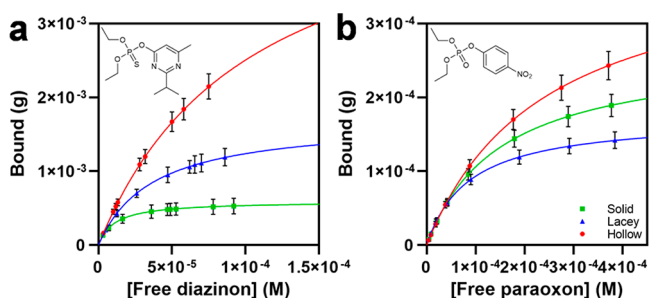


**Figure 5.** Binding of diazinon and paraoxon by solid (S-AMNP), lacey (L-AMNP), and hollow (H-AMNP) nanoparticles. (a) Diazinon adsorption. (b) Paraoxon adsorption. Error bars represent the standard deviation based on three replicate measures.

Binding data suggest that L-AMNP (41.4 g/g) is more efficient at binding diazinon than S-AMNP (14.5 g/g), but not paraoxon (L-AMNP 4.2 g/g and S-AMNP 6.5 g/g). Surprisingly, despite H-AMNPs having similar surface areas to S-AMNPs, they are capable of binding both diazinon (124 g/g) and paraoxon (9.8 g/g) better than S- or L-AMNPs. This suggests that surface area is not the only parameter important for diazinon binding, which corroborates the higher affinity for diazinon seen in S-AMNP (91305 $M^{-1}$ vs 27310 $M^{-1}$ for L-AMNP and 9739 $M^{-1}$ for H-AMNP). However, surface area trends are consistent with paraoxon affinities (4162 $M^{-1}$ for H-AMNP, 6698 $M^{-1}$ for S-AMNP, and 11658 $M^{-1}$ for L-AMNP). Results from these studies can be found summarized in Table S4. The performance of these materials in on par with that of porous organosilicates.[43]

**Toxin Adsorption on Nylon−Cotton (NYCO) AMNP-Coated Fabrics.** We next applied AMNPs to nylon−cotton (NYCO) fabric and tested their ability to withstand breakthrough following dimethyl methylphosphonate (DMMP) exposure (Figure 6). DMMP is an analogue of sarin gas and a common simulant for phosphorus containing nerve agents and for permeation studies due to its stability in the gas phase

at room temperature.[42] Despite the fact that production and stockpiling of sarin and similar nerve agents have been outlawed, they remain in use as chemical warfare agents.[44,45] Antidotes are available, but they must be administered very quickly after exposure and may not be widely accessible. Clothing with the ability to slow and/or impede the permeation of nerve agents may provide sufficiently increased protection and/or time necessary to obtain antidotes and treatment. To this end, NYCO swatches (2.5 $cm^2$) were coated (dyed) by immersion in a suspension of AMNPs (4 mg/mL) or a 1,8-DHN monomer solution (4 mg/mL), stirred at 45 °C for 15 h, and then washed and dried thoroughly (Figure 6a). AMNP-coated fabric swatches (S-AMNP-NYCO, L-AMNP-NYCO, or H-AMNP-NYCO for S-AMNP, L-AMNP, and H-AMNP, respectively) were imaged via SEM to illustrate the distribution of material along the fibers, with individual nanoparticles visible for each sample, in comparison to 1,8-DHN-coated (DHN-NYCO) and uncoated (CTRL-NYCO) controls (Figure 6b−d and Figure S27). Fabric swatches were then tested for permeability to DMMP by using a stainless-steel aerosol−vapor−liquid−assessment group (AVLAG) cell which holds the sample horizontally with O-ring seals, supported with solid disks. Liquid droplets of DMMP were applied to the top of the fabric by using a repeating dispenser and a flame ionization detector (FID) continuously monitored DMMP concentration on the bottom of the fabric over 16 h. Typically, the threshold used for initial target breakthrough is based on the military exposure guideline (MEG) of 1 h of marginal exposure level in air. A "marginal" hazard level is defined as causing degraded mission capability or unit readiness. This is based on the proportion of the unit likely to exhibit effects, the nature of those effects, and confidence in the available data. The 1 h marginal air exposure limit for DMMP is 500 $mg/m^3$.[46] None of the materials evaluated permitted target breakthrough at this rate (Figure 6e). To provide a point of comparison, 5.0 $mg/m^3$ was used as the threshold value for DMMP analysis. The peak DMMP rate through CTRL-NYCO was 7.5 g/($m^2$ h) with initial breakthrough at <1 min and 1030 $\mu$g recovered over the 1000 min experiment duration. DHN-NYCO swatches had no impact on initial breakthrough (<1.0 min) but resulted in a higher peak transport rate of 10.9 g/($m^2$ h), with a similar final recovery of 1027 $\mu$g. S-AMNP-NYCO delayed DMMP breakthrough to 25.2 min and resulted in a recovery of 981 $\mu$g with a peak rate of 10.02 g/($m^2$ h). Both L-AMNP-NYCO and H-AMNP-NYCO had significantly improved performance over S-AMNP-NYCO, DHN-NYCO, and CTRL-NYCO. DMMP permeation through L-AMNP-NYCO and H-AMNP-NYCO remained below the 5.0 $mg/m^3$ peak rate threshold, and their peak rates were low, at 0.53 and 0.50 g/($m^2$ h), respectively. The total transport was 124 $\mu$g for L-AMNP-NYCO and 160 $\mu$g for H-AMNP-NYCO—an order of magnitude lower than CTRL-NYCO and DHN-NYCO controls. Although other fabric coatings exist that have exceptional DMMP resistance, they are not always practical. StedCarb, for example, exhibits complete resistance to DMMP; however, the material also impedes permeation of water vapor, a proxy for breathability in fabrics.[47] Fabrics that do not permit water vapor transport are uncomfortable for the wearer and suitable for short duration use only. We sought to examine all NYCO fabric swatches to see whether they exhibited efficient water vapor transport, comparing these values to that of a polytetrafluoroethylene (PTFE) membrane control which is
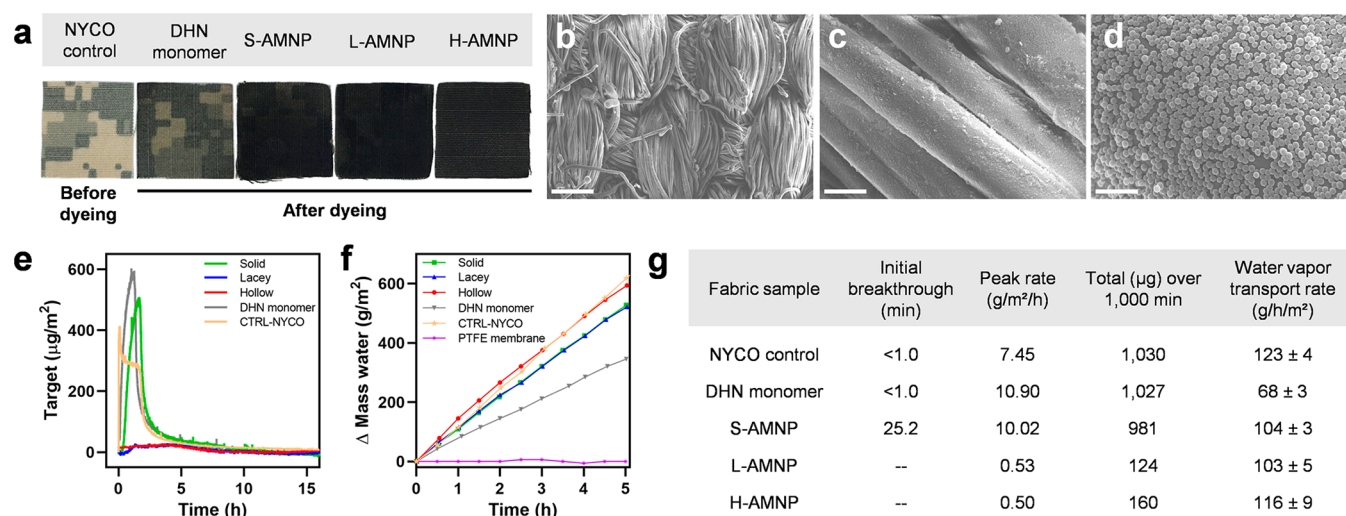
**Figure 6.** AMNP-coated nylon−cotton (NYCO) fabric toxin permeation studies. (a) Photographs of 2.5 cm$^2$ NYCO swatches before and after coating with AMNPs or 1,8-DHN monomer. (b−d) SEM images of H-AMNP-NYCO. Scale bars: (b) 200 $\mu$m, (c) 10 $\mu$m, and (d) 1 $\mu$m. (e) Time-dependent FID response of dimethyl methylphosphonate (DMMP) permeating through NYCO coated and uncoated fabric swatches. (f) Water vapor transport across NYCO coated and uncoated fabric swatches vs polytetrafluoroethylene (PTFE) control membrane. (g) Breakthrough times, rates, and total masses for DMMP exposure and water vapor transport rates across NYCO fabrics.

highly fluorinated and nonpermeable to water vapor (Figure 6f). All AMNP-NYCO and CTRL-NYCO showed similar water vapor transport, indicating that the coatings should have little impact on comfort, and the PTFE performed as expected, with essentially zero transport of water vapor. Interestingly, DHN-NYCO, which performed poorly in the DMMP breakthrough study, was less permeable to water vapor than AMNP-NYCO or CTRL-NYCO, although still much more permeable than PTFE. These results are promising for the application of AMNPs as active dyes for uniforms or other fabrics where the wearer is in need of additional protection (Figure 6g). The black color of the dyes may additionally be useful for certain applications, and for others, they can potentially be used to coat inner layers of multilayer, composite fabrics.

**Porosity and Toxin Adsorption of Fungal Melanin Microstructures.** Returning to the original inspiration from naturally melanized systems, we sought a natural analogue to determine if they possessed any similarities or promising attributes with respect to porosity and adsorption properties. Our candidate material was the melanized hollow shell created by the etching of fungal cells that constitutively synthesize DHN melanin. These structures are known as melanin ghosts, with a more complex chemical makeup compared to our solely DHN-derived synthetic systems, containing a mixture of 1,8-DHN and related compounds as well as cellular components.[48,49] These structures were imaged by using SEM and TEM, followed by porosity measurements (Figure 7). To make the fungal ghosts, fungal cell walls were enzymatically lysed, followed by treatment with guanidine thiocyanate, proteinase-K, and then 6 M HCl (Figure 7a). They were washed in water to afford the hollow ghost structures. The cell culture supernatant was precipitated in 0.6 M HCl to afford melanin aggregates, imaged via SEM (Figure 7b). These particles were found to be relatively nonporous, with a BET area of 15 m$^2$/g. Melanin ghosts were also imaged via SEM (Figure 7c,d) and STEM (Figure 7e). SEM samples were prepared by fixation, dehydration in ethanol, and critical point drying in CO$_2$ to preserve the solvated structure. Nitrogen isotherms indicate

the ghosts have a non-negligible surface area of 95 m$^2$/g (Figure 7f) with an average micropore pore size of 13.5 Å (Figure 7g). Intriguingly, the fungal ghosts provided binding capacity larger than S-AMNP and L-AMNP for both paraoxon and diazinon but less than that of H-AMNP. The binding affinities were within the ranges noted for AMNPs (Figure S28). With the heterogeneous nature of the fungal melanin (that is, they contain cellular components including chitin and glucan), it is not possible to say what the contribution of allomelanin itself is to the observed porosity. Regardless, these results beg the question whether melanized organisms in nature might have high porosities, dependent on the abundance of certain chemical precursors. This is evidence that while not as porous as the pure synthetic allomelanin analogues, there is promise for the discovery of other biopolymers of intrinsic microporosity (BioPIMs) in nature.

## CONCLUSION

We found that the initially formed allomelanin nanoparticles, assembled from low molecular weight oligomers, undergo further oxidation and chemical cross-linking on a time scale that allows for partial dissolution resulting in tunable morphology and porosity. Similar structures can be made biosynthetically by etching melanized bacterial or fungal cells to afford hollow structures called melanin ghosts, albeit on a different length scale.[50] Here, we show that the synthesis of these porous AMNP structures is facile and template-free and requires few starting materials, all of which are commercially available with the principal component, 1,8-DHN, being naturally occurring. In addition, the synthesis can easily be adjusted with a simple MeOH treatment to enable tunable morphology and increased porosity, while retaining high uniformity.

The initially observed solvent instability and visible color change over time in AMNPs allowed us to consider the possibility of chemical tunability. A solvent screen and time series of MeOH treatment revealed a structure that when first synthesized contains a loosely associated core of oligomers which are disrupted by organic solvent and can leach out of the
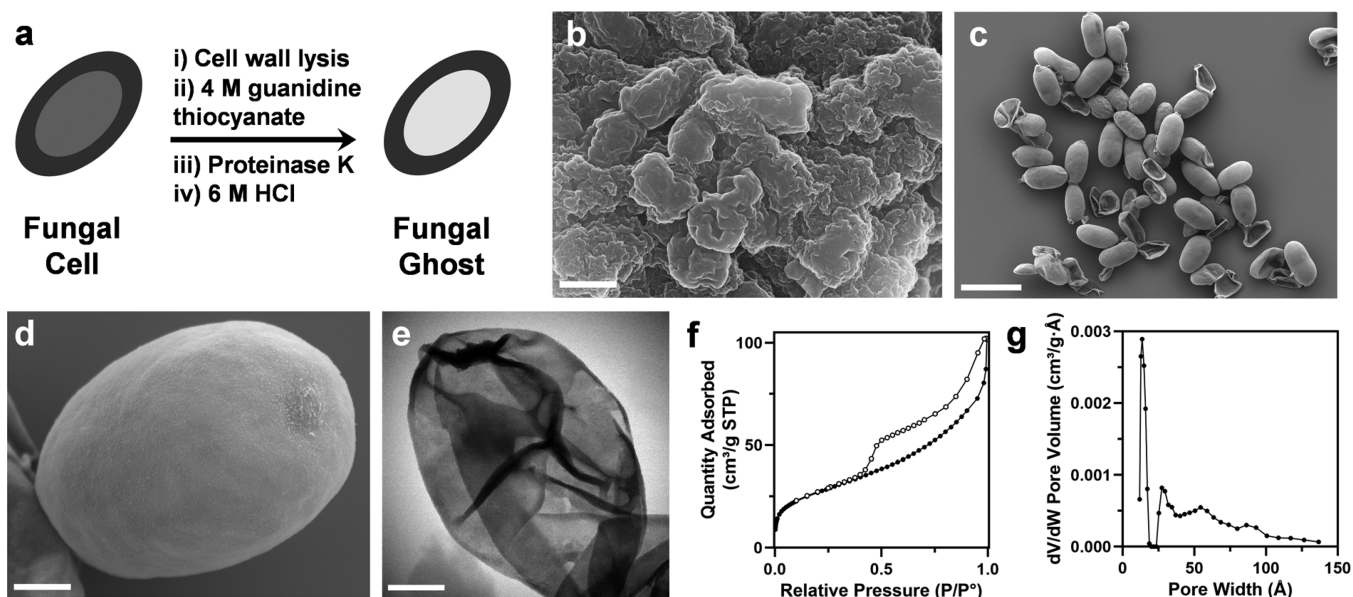
**Figure 7.** Melanized fungal cell ghost synthesis and characterization. (a) Schematic of the melanin ghost formation process. (b) SEM image of aggregates precipitated in HCl from cell culture supernatant (scale bar: 500 nm). (c) SEM image of ghosts after critical point drying (scale bar: 10 $\mu$m). (d) Zoom-in SEM image of ghost after critical point drying (scale bar: 1 $\mu$m). (e) STEM image of ghost (scale bar: 1 $\mu$m). (f) $N_2$ isotherm of ghosts, which yields a BET area of 95 $m^2$/g. Closed markers represent adsorption, and open markers represent desorption. (g) Ghost pore size distribution, with an average micropore size of 13.5 Å.

particle and be redeposited onto the surface over several days. This is consistent with a general increase in size from S- to L- to H-AMNP, as revealed by STEM, AFM, and SAXS analyses. To clarify whether there was a conservation of material between AMNPs, the total particle intensity was normalized by area. Irrespective of their morphology, each AMNP contains approximately the same amount of material. This is consistent with the mechanism of formation of L- and H-AMNPs leaching oligomers from their cores and redepositing them onto the particle surface, growing the outer diameters of the particles by using material leached from the core. In addition, the high uniformity of the three AMNPs enabled 3D modeling from well-formed SAXS scattering curves, often reserved for highly ordered, crystalline systems.

BET measurements revealed AMNPs have high surface areas with tunable micropores capable of adsorbing $N_2$, $CH_4$, and $CO_2$. The functionalized surface of these materials also proved to be advantageous for ammonia capture, with results on par or surpassing capabilities of highly ordered, crystalline structures such as MOFs.[28−31] AMNPs were also capable of adsorbing the toxin simulants diazinon and paraoxon in solution and were highly efficient at preventing the permeation of DMMP across AMNP-coated NYCO fabric while allowing the transport of water vapor. This breathable yet absorbent material could be generated in a straightforward manner with a simple deposition method from materials that are stable at room temperature in water for at least 18 months prior to use.

This work demonstrates how simple materials generated from biologically relevant building blocks may provide a route to scalable, biocompatible materials for applications such as toxin remediation and gas adsorption. In addition, it proposes the intriguing possibility that such porosity exists for natural melanins or other biomaterials yet to be discovered. With this inspiration in mind, we showed that natural allomelanin-containing hollow structures (fungal ghosts) have non-negligible porosity with the capability to adsorb diazinon and

paraoxon toxins, and that in the future other porous melanins might be discovered. These results beg the question whether allomelanin-containing organisms in nature might utilize this high porosity to their evolutionary advantage. Indeed, some melanins are known to be toxin adsorbents in organisms, yet they are not known to have high surface areas, and have not been described in terms of their microporosity,[7,8] although some suggestion of porosity has been evidenced by NMR cryoporometry studies probing fungal eumelanin ghosts.[51] However, fungal melanin is not known to exist in a pure state in the cell wall but rather is incorporated with other cell wall components such as polysaccharides and chitin, and the amount of DHN in allomelanin-containing fungal cells has yet to be quantified.[17,18] Future work will aim to quantify the melanin composition and attempt to manipulate the biochemistry of these organisms to clearly elucidate the contributions of DHN to the overall structure and function. Synthesis provides a facile approach to access and probe the performance of pure DHN–melanin devoid of confounding biological structures and molecules from the natural system, with the understanding that these additional materials may provide essential biological functions. Moreover, this synthetic allomelanin may inspire further investigation of microporosity of this type in natural biopolymers originating with fungi and extending to other organisms. Finally, in synthetic systems, this kind of bioinspired approach to porous materials could complement the sophisticated designed materials that have become of increasing interest in the form of metal−organic frameworks (MOFs),[52,53] covalent organic frameworks (COFs),[54,55] and mixed matrix membranes.[56,57]

## ■ EXPERIMENTAL SECTION

**Synthesis of Allomelanin Nanoparticles.** Solid (S-AMNPs) were synthesized largely based on the protocol for "AMNP-1" from previous work.[21] Briefly, 150 mg of 1,8-DHN was dissolved in 7.5 mL of acetonitrile (ACN) and then 142.5 mL of Milli-Q water was added. The mixture was stirred for 5 min at room temperature, and then 1

mL of 1 N $NaIO_4$ was quickly injected into the solution while stirring vigorously. After 20 h, the solution was washed three times in Milli-Q water by centrifugation at 11500 rpm for 10 min.

Hollow (H-AMNPs) were synthesized from a fresh batch of purified S-AMNP which were left in a closed tube (containing ambient air) on the benchtop for 24 h. They were centrifuged at 11500 rpm for 10 min to remove water and then resuspended in MeOH at 0.5 mg/mL. The suspension was agitated for 6 days and then dialyzed into Milli-Q water.

Lacey (L-AMNPs) were synthesized from a fresh batch of purified S-AMNP which were left in a closed tube (containing ambient air) on the benchtop for 48 h. They were centrifuged at 11500 rpm for 10 min to remove water and then resuspended in MeOH at 0.5 mg/mL. The suspension was agitated for 6 days and then dialyzed into Milli-Q water.

**Small-Angle X-ray Scattering (SAXS) Studies.** Experiments were performed at beamline 5-ID-D of the DuPont−Northwestern−Dow Collaborative Access Team (DND-CAT) Synchrotron Research Center at the Advanced Photon Source (APS), Argonne National Laboratory. AMNPs were prepared at 10 mg/mL in Milli-Q water and during measurements flowed through a 1.5 mm glass capillary at 1 mm/s for consistent background subtraction. Data were collected with X-ray energy at 17 keV ($\lambda = 0.73$ Å) with samples exposed for 10 frames of 0.2 s each. Modeling of the scattering data with a spherical core−shell geometrical model was conducted in the Irena software package running on IgorPro software.[58] Scattering data were also assessed by using *ab initio* dummy atom modeling (DAM) methods using the ATSAS analysis software.[27]

**Sorption Measurements.** AMNPs were solvent switched into EtOH and critically activated prior to measurements. Nitrogen physisorption measurements were collected by using a Micromeritics ASAP 2020 instrument at 77 K. Pore-size distributions were obtained by using DFT calculations with a carbon slit geometry and an $N_2$ DFT model. $CO_2$ and $CH_4$ isotherms were measured by using a Micromeritics ASAP 2020 instrument at 298 K. $NH_3$ isotherms were collected by using a Micromeritics 3Flex Physisorption instrument at 298 K. Ideal adsorbed solution theory (IAST) calculations and isotherm fittings using a BET model for $CO_2/CH_4$ were performed by using the Python package pyIAST.[35]

**Toxin Binding Studies.** Paraoxon and diazinon solutions were prepared in Milli-Q water at varied concentration (1−100 ppm). AMNPs were added to the target solution in a scintillation vial (total volume 20 mL with masses of 40, 20, and 10 $\mu$g ± 1 $\mu$g). Samples were mixed on a rotisserie mixer for 2 h in the dark at room temperature; they were then filtered by using 0.2 mm PTFE syringe filters. Analysis of the target remaining in the sample was completed by HPLC. The resulting data were fit by using the Langmuir isotherm to generate the saturation loading for the materials in grams/gram and an affinity coefficient (1/M).

**Nylon−Cotton (NYCO) Fabric Studies.** Fabric swatches (2.5 $cm^2$) were immersed in 4 mg/mL AMNPs in water or 4 mg/mL 1,8-DHN monomer in water, stirred at 45 °C for 15 h, and then dried. Permeation of dimethyl methylphosphonate (DMMP) was assessed as described by Test Operations Procedure (TOP) 8-2-501, Permeation Testing of Materials with Chemical Agents or Simulants (Swatch Testing).[46,59] The target was placed in the headspace above the fabric swatch, supported between two discs. This assembly was then placed in a stainless-steel aerosol−vapor−liquid−assessment group (AVLAG) cell and humidity equilibrated for 2 h. DMMP was applied as liquid droplets by using a repeating dispenser, and the concentration was monitored by using a dedicated flame ionization detector (FID). The water vapor transport (WVT) rate for the treated fabrics was evaluated by using a circular fabric sample with a total exposed area of 1.65 $cm^2$.[46,60,61] This method follows the guidance provided by ASTM E96, Water Vapor Transport: Upright Open Cup Method to characterize water vapor transport through the fabric samples. The fabric sample was sealed over a preweighed vial. A desiccant was used to drive a humidity differential in the incubator, with a dry nitrogen stream flowing across the surface of the sample

(0.25 L/min). The weight of the vial was measured at 30−45 min intervals by using an analytical balance.

## ASSOCIATED CONTENT

**SI Supporting Information**

The Supporting Information is available free of charge at https://pubs.acs.org/doi/10.1021/jacs.1c00748.

Additional methods, UV−vis, STEM timeseries, DLS, zeta potential titration, reaction schematic, SAXS modeling and parameters, DAMMIF modeling runs, pure component isotherms, SEM of NYCO fabrics, fungal ghost toxin adsorption (PDF)

Video S1 (MP4)

Video S2 (MP4)

Video S3 (MP4)

Video S4 (MP4)

## AUTHOR INFORMATION

**Corresponding Author**

**Nathan C. Giannneschi** − *Department of Chemistry, International Institute for Nanotechnology (IIN), Simpson Querrey Institute, Department of Materials Science and Engineering, Department of Biomedical Engineering, Chemistry of Life Processes Institute, and Lurie Cancer Center, Northwestern University, Evanston, Illinois 60208, United States; Department of Chemistry & Biochemistry, University of California, San Diego, La Jolla, California 92093, United States;* orcid.org/0000-0001-9945-5475; Email: nathan.giannneschi@northwestern.edu

**Authors**

**Naneki C. McCallum** − *Department of Chemistry and International Institute for Nanotechnology (IIN), Northwestern University, Evanston, Illinois 60208, United States;* orcid.org/0000-0001-9210-3493

**Florencia A. Son** − *Department of Chemistry and International Institute for Nanotechnology (IIN), Northwestern University, Evanston, Illinois 60208, United States;* orcid.org/0000-0002-7524-3774

**Tristan D. Clemons** − *Department of Chemistry and Simpson Querrey Institute, Northwestern University, Evanston, Illinois 60208, United States;* orcid.org/0000-0001-8042-0141

**Steven J. Weigand** − *DuPont−Northwestern−Dow Collaborative Access Team (DND-CAT) Synchrotron Research Center, Northwestern University, Argonne, Illinois 60208, United States*

**Karthikeyan Gnanasekaran** − *Department of Chemistry and International Institute for Nanotechnology (IIN), Northwestern University, Evanston, Illinois 60208, United States;* orcid.org/0000-0001-6635-0888

**Claudia Battistella** − *Department of Chemistry and International Institute for Nanotechnology (IIN), Northwestern University, Evanston, Illinois 60208, United States;* orcid.org/0000-0002-5426-6205

**Brooke E. Barnes** − *George & Josephine Butler Polymer Research Laboratory, Center for Macromolecular Science & Engineering, Department of Chemistry, University of Florida, Gainesville, Florida 32611, United States*

**Hashanthi Abeyratne-Perera** − *American Society for Engineering Education Postdoctoral Research Associate, US Naval Research Laboratory, Washington, D.C. 20375, United States*

**Zofia E. Siwicka** − *Department of Chemistry and International Institute for Nanotechnology (IIN), Northwestern University, Evanston, Illinois 60208, United States;* ● orcid.org/0000-0002-6028-5306

**Christopher J. Forman** − *Department of Chemistry and International Institute for Nanotechnology (IIN), Northwestern University, Evanston, Illinois 60208, United States*

**Xuhao Zhou** − *Department of Chemistry and International Institute for Nanotechnology (IIN), Northwestern University, Evanston, Illinois 60208, United States;* ● orcid.org/0000-0002-7181-607X

**Martin H. Moore** − *Center for Bio/Molecular Science & Engineering, US Naval Research Laboratory, Washington, D.C. 20375, United States*

**Daniel A. Savin** − *George & Josephine Butler Polymer Research Laboratory, Center for Macromolecular Science & Engineering, Department of Chemistry, University of Florida, Gainesville, Florida 32611, United States*

**Samuel I. Stupp** − *Department of Chemistry, Simpson Querrey Institute, Department of Materials Science and Engineering, Department of Biomedical Engineering, and Department of Medicine, Northwestern University, Evanston, Illinois 60208, United States;* ● orcid.org/0000-0002-5491-7442

**Zheng Wang** − *Center for Bio/Molecular Science & Engineering, US Naval Research Laboratory, Washington, D.C. 20375, United States*

**Gary J. Vora** − *Center for Bio/Molecular Science & Engineering, US Naval Research Laboratory, Washington, D.C. 20375, United States;* ● orcid.org/0000-0002-0657-8597

**Brandy J. Johnson** − *Center for Bio/Molecular Science & Engineering, US Naval Research Laboratory, Washington, D.C. 20375, United States;* ● orcid.org/0000-0002-3637-0631

**Omar K. Farha** − *Department of Chemistry, International Institute for Nanotechnology (IIN), and Department of Chemical and Biological Engineering, Northwestern University, Evanston, Illinois 60208, United States;* ● orcid.org/0000-0002-9904-9845

Complete contact information is available at:
https://pubs.acs.org/10.1021/jacs.1c00748

**Author Contributions**

This manuscript was written through contributions of all authors. All authors have given approval to the final version of the manuscript.

**Notes**

The authors declare no competing financial interest.

## ■ ABBREVIATIONS

AFM, atomic force microscopy; AMNP, artificial allomelanin nanoparticle; AVLAG, aerosol−vapor−liquid−assessment group; BET, Brunauer−Emmett−Teller; BF, bright-field; DAM, dummy atom modeling; DHN, dihydroxynaphthalene; DLS, dynamic light scattering; DMMP, dimethyl methyl-phosphonate; FID, flame ionization detector; HAADF, high-angle annular dark-field; H-AMNP, hollow AMNP; IAST, ideal adsorbed solution theory; ID, inner diameter; L-AMNP, lacey AMNP; NYCO, nylon−cotton; OD, outer diameter; PDA, polydopamine; S-AMNP, solid AMNP; SAXS, small-angle X-ray scattering; SEM, scanning electron microscopy; SLS, static light scattering; STEM, scanning transmission electron microscopy.

## ■ REFERENCES

(1) D'Alba, L.; Shawkey, M. D. Melanosomes: Biogenesis, Properties, and Evolution of an Ancient Organelle. *Physiol. Rev.* **2019**, *99* (1), 1−19.

(2) Pacelli, C.; Bryan, R. A.; Onofri, S.; Selbmann, L.; Shuryak, I.; Dadachova, E. Melanin is effective in protecting fast and slow growing fungi from various types of ionizing radiation. *Environ. Microbiol.* **2017**, *19* (4), 1612−1624.

(3) Hong, L.; Simon, J. D. Current understanding of the binding sites, capacity, affinity, and biological significance of metals in melanin. *J. Phys. Chem. B* **2007**, *111* (28), 7938−7947.

(4) Riley, P. A. A proposed selective mechanism based on metal chelation in industrial melanic moths. *Biol. J. Linn. Soc.* **2013**, *109* (2), 298−301.

(5) Rogalla, S.; D'Alba, L.; Verdoodt, A.; Shawkey, M. D. Hot wings: thermal impacts of wing coloration on surface temperature during bird flight. *J. R. Soc., Interface* **2019**, *16* (156), 20190032.

(6) Stoddard, M. C.; Prum, R. O. How colorful are birds? Evolution of the avian plumage color gamut. *Behav Ecol* **2011**, *22* (5), 1042−1052.

(7) Goiran, C.; Bustamante, P.; Shine, R. Industrial Melanism in the Seasnake Emydocephalus annulatus. *Curr. Biol.* **2017**, *27* (16), 2510−2513.

(8) Price, R. J.; Lee, J. S. Paralytic Shellfish Poison and Melanin Distribution in Fractions of Toxic Butter Clam (Saxidomus-Giganteus) Siphon. *J. Fish. Res. Board Can.* **1972**, *29* (11), 1657−1658.

(9) Lee, B. P.; Messersmith, P. B.; Israelachvili, J. N.; Waite, J. H. Mussel-Inspired Adhesives and Coatings. *Annu. Rev. Mater. Res.* **2011**, *41*, 99−132.

(10) Liu, Y. L.; Ai, K. L.; Lu, L. H. Polydopamine and Its Derivative Materials: Synthesis and Promising Applications in Energy, Environmental, and Biomedical Fields. *Chem. Rev.* **2014**, *114* (9), 5057−5115.

(11) Lynge, M. E.; van der Westen, R.; Postma, A.; Stadler, B. Polydopamine-a nature-inspired polymer coating for biomedical science. *Nanoscale* **2011**, *3* (12), 4916−4928.

(12) Ju, K.-Y.; Lee, Y.; Lee, S.; Park, S. B.; Lee, J.-K. Bioinspired Polymerization of Dopamine to Generate Melanin-Like Nanoparticles Having an Excellent Free-Radical-Scavenging Property. *Biomacromolecules* **2011**, *12* (3), 625−632.

(13) Cao, W.; Zhou, X.; McCallum, N. C.; Hu, Z.; Ni, Q. Z.; Kapoor, U.; Heil, C. M.; Cay, K. S.; Zand, T.; Mantanona, A. J.; Jayaraman, A.; Dhinojwala, A.; Deheyn, D. D.; Shawkey, M. D.; Burkart, M. D.; Rinehart, J. D.; Gianneschi, N. C. Unraveling the Structure and Function of Melanin through Synthesis. *J. Am. Chem. Soc.* **2021**, DOI: 10.1021/jacs.0c12322.

(14) Cui, J. W.; Wang, Y. J.; Postma, A.; Hao, J. C.; Hosta-Rigau, L.; Caruso, F. Monodisperse Polymer Capsules: Tailoring Size, Shell Thickness, and Hydrophobic Cargo Loading via Emulsion Templating. *Adv. Funct. Mater.* **2010**, *20* (10), 1625−1631.

(15) Yi, B.; Shen, H. F. Liquid-immune structural colors with angle-independence inspired from hollow melanosomes. *Chem. Commun.* **2017**, *53* (66), 9234−9237.

(16) Wang, Y.; Su, J.; Li, T.; Ma, P. M.; Bai, H. Y.; Xie, Y.; Chen, M. Q.; Dong, W. F. A Novel UV-Shielding and Transparent Polymer Film: When Bioinspired Dopamine-Melanin Hollow Nanoparticles Join Polymers. *ACS Appl. Mater. Interfaces* **2017**, *9* (41), 36281−36289.

(17) Chatterjee, S.; Prados-Rosales, R.; Itin, B.; Casadevall, A.; Stark, R. E. Solid-state NMR Reveals the Carbon-based Molecular Architecture of Cryptococcus neoformans Fungal Eumelanins in the Cell Wall. *J. Biol. Chem.* **2015**, *290* (22), 13779−13790.

(18) Zhong, J. Y.; Frases, S.; Wang, H.; Casadevall, A.; Stark, R. E. Following fungal melanin biosynthesis with solid-state NMR: Biopolyrner molecular structures and possible connections to cell-wall polysaccharides. *Biochemistry* **2008**, *47* (16), 4701−4710.

(19) Manini, P.; Lino, V.; Franchi, P.; Gentile, G.; Sibillano, T.; Giannini, C.; Picardi, E.; Napolitano, A.; Valgimigli, L.; Chiappe, C.; D'Ischia, M. A Robust Fungal Allomelanin Mimic: An Antioxidant and Potent pi-Electron Donor with Free-Radical Properties that can be Tuned by Ionic Liquids. *ChemPlusChem.* **2019**, *84* (9), 1331−1337.

(20) Cecchini, M. M.; Reale, S.; Manini, P.; d'Ischia, M.; De Angelis, F. Modeling Fungal Melanin Buildup: Biomimetic Polymerization of 1,8-Dihydroxynaphthalene Mapped by Mass Spectrometry. *Chem. - Eur. J.* **2017**, *23* (33), 8092−8098.

(21) Zhou, X. H.; McCallum, N. C.; Hu, Z. Y.; Cao, W.; Gnanasekaran, K.; Feng, Y. N.; Stoddart, J. F.; Wang, Z.; Gianneschi, N. C. Artificial Allomelanin Nanoparticles. *ACS Nano* **2019**, *13* (10), 10980−10990.

(22) Budd, P. M.; Ghanem, B. S.; Makhseed, S.; McKeown, N. B.; Msayib, K. J.; Tattershall, C. E. Polymers of intrinsic microporosity (PIMs): robust, solution-processable, organic nanoporous materials. *Chem. Commun. (Cambridge, U. K.)* **2004**, No. 2, 230−1.

(23) Li, C. Y.; Ward, A. L.; Doris, S. E.; Pascal, T. A.; Prendergast, D.; Helms, B. A. Polysulfide-Blocking Microporous Polymer Membrane Tailored for Hybrid Li-Sulfur Flow Batteries. *Nano Lett.* **2015**, *15* (9), 5724−5729.

(24) Weng, X. L.; Baez, J. E.; Khiterer, M.; Hoe, M. Y.; Bao, Z. B.; Shea, K. J. Chiral Polymers of Intrinsic Microporosity: Selective Membrane Permeation of Enantiomers. *Angew. Chem., Int. Ed.* **2015**, *54* (38), 11214−11218.

(25) Kapoor, U.; Jayaraman, A. Self-Assembly of Allomelanin Dimers and the Impact of Poly(ethylene glycol) on the Assembly: A Molecular Dynamics Simulation Study. *J. Phys. Chem. B* **2020**, *124* (13), 2702−2714.

(26) Manini, P.; Lino, V.; D'Errico, G.; Reale, S.; Napolitano, A.; De Angelis, F.; d'Ischia, M. "Blackness" is an index of redox complexity in melanin polymers. *Polym. Chem.* **2020**, *11* (31), 5005−5010.

(27) Franke, D.; Petoukhov, M. V.; Konarev, P. V.; Panjkovich, A.; Tuukkanen, A.; Mertens, H. D. T.; Kikhney, A. G.; Hajizadeh, N. R.; Franklin, J. M.; Jeffries, C. M.; Svergun, D. I. ATSAS 2.8: a comprehensive data analysis suite for small-angle scattering from macromolecular solutions. *J. Appl. Crystallogr.* **2017**, *50*, 1212−1225.

(28) Moribe, S.; Chen, Z. J.; Alayoglu, S.; Syed, Z. H.; Islamoglu, T.; Farha, O. K. Ammonia Capture within Isoreticular Metal-Organic Frameworks with Rod Secondary Building Units. *ACS Mater. Lett.* **2019**, *1* (4), 476−480.

(29) Rieth, A. J.; Dinca, M. Controlled Gas Uptake in Metal-Organic Frameworks with Record Ammonia Sorption. *J. Am. Chem. Soc.* **2018**, *140* (9), 3461−3466.

(30) Chen, Y. W.; Zhang, X.; Ma, K. K.; Chen, Z. J.; Wang, X. J.; Knapp, J.; Alayoglu, S.; Wang, F. F.; Xia, Q. B.; Li, Z.; Islamoglu, T.; Farha, O. K. Zirconium-Based Metal-Organic Framework with 9-Connected Nodes for Ammonia Capture. *ACS Appl. Nano Mater.* **2019**, *2* (10), 6098−6102.

(31) Chen, Z.; Wang, X.; Cao, R.; Idrees, K. B.; Liu, X.; Wasson, M. C.; Farha, O. K. Water-Based Synthesis of a Stable Iron-Based Metal−Organic Framework for Capturing Toxic Gases. *ACS Mater. Lett.* **2020**, *2*, 1129−1134.

(32) Van Humbeck, J. F.; McDonald, T. M.; Jing, X.; Wiers, B. M.; Zhu, G.; Long, J. R. Ammonia capture in porous organic polymers densely functionalized with Bronsted acid groups. *J. Am. Chem. Soc.* **2014**, *136* (6), 2432−40.

(33) Barin, G.; Peterson, G. W.; Crocella, V.; Xu, J.; Colwell, K. A.; Nandy, A.; Reimer, J. A.; Bordiga, S.; Long, J. R. Highly effective ammonia removal in a series of Bronsted acidic porous polymers: investigation of chemical and structural variations. *Chem. Sci.* **2017**, *8* (6), 4399−4409.

(34) Dawson, R.; Stockel, E.; Holst, J. R.; Adams, D. J.; Cooper, A. I. Microporous organic polymers for carbon dioxide capture. *Energy Environ. Sci.* **2011**, *4* (10), 4239−4245.

(35) Simon, C. M.; Smit, B.; Haranczyk, M. pyIAST: Ideal adsorbed solution theory (IAST) Python package. *Comput. Phys. Commun.* **2016**, *200*, 364−380.

(36) Spanopoulos, I.; Xydias, P.; Malliakas, C. D.; Trikalitis, P. N. A Straight Forward Route for the Development of Metal-Organic Frameworks Functionalized with Aromatic -OH Groups: Synthesis, Characterization, and Gas (N-2, Ar, H-2, $CO_2$, CH4, NH3) Sorption Properties. *Inorg. Chem.* **2013**, *52* (2), 855−862.

(37) Chen, Z. X.; Xiang, S. C.; Arman, H. D.; Li, P.; Zhao, D. Y.; Chen, B. L. Significantly Enhanced $CO_2$/CH4 Separation Selectivity within a 3D Prototype Metal-Organic Framework Functionalized with OH Groups on Pore Surfaces at Room Temperature. *Eur. J. Inorg. Chem.* **2011**, *2011* (14), 2227−2231.

(38) Venna, S. R.; Carreon, M. A. Highly permeable zeolite imidazolate framework-8 membranes for $CO_2$/CH4 separation. *J. Am. Chem. Soc.* **2010**, *132* (1), 76−8.

(39) Li, Y.; Wang, S.; Wang, B.; Wang, Y.; Wei, J. Sustainable Biomass Glucose-Derived Porous Carbon Spheres with High Nitrogen Doping: As a Promising Adsorbent for $CO_2$/CH4/N2 Adsorptive Separation. *Nanomaterials* **2020**, *10* (1), 174.

(40) Bae, Y. S.; Mulfort, K. L.; Frost, H.; Ryan, P.; Punnathanam, S.; Broadbelt, L. J.; Hupp, J. T.; Snurr, R. Q. Separation of $CO_2$ from CH4 using mixed-ligand metal-organic frameworks. *Langmuir* **2008**, *24* (16), 8592−8.

(41) Bartelt-Hunt, S. L.; Knappe, D. R. U.; Barlaz, M. A. A review of chemical warfare agent simulants for the study of environmental behavior. *Crit. Rev. Environ. Sci. Technol.* **2008**, *38* (2), 112−136.

(42) Kim, K.; Tsay, O. G.; Atwood, D. A.; Churchill, D. G. Destruction and Detection of Chemical Warfare Agents. *Chem. Rev.* **2011**, *111* (9), 5345−5403.

(43) Johnson, B. J.; Malanoski, A. P.; Leska, I. A.; Melde, B. J.; Taft, J. R.; Dinderman, M. A.; Deschamps, J. R. Adsorption of organophosphates from solution by porous organosilicates: Capillary phase-separation. *Microporous Mesoporous Mater.* **2014**, *195*, 154−160.

(44) Dolgin, E. Syrian gas attack reinforces need for better anti-sarin drugs. *Nat. Med.* **2013**, *19* (10), 1194−1195.

(45) John, H.; van der Schans, M. J.; Koller, M.; Spruit, H. E. T.; Worek, F.; Thiermann, H.; Noort, D. Fatal sarin poisoning in Syria 2013: forensic verification within an international laboratory network. *Forensic Toxicol.* **2018**, *36* (1), 61−71.

(46) Martin, B. D.; Justin, G. A.; Moore, M. H.; Naciri, J.; Mazure, T.; Melde, B. J.; Stroud, R. M.; Ratna, B. An Elastomeric Poly(Thiophene-EDOT) Composite with a Dynamically Variable Permeability Towards Organic and Water Vapors. *Adv. Funct. Mater.* **2012**, *22* (15), 3116−3127.

(47) Wang, S.; Pomerantz, N. L.; Dai, Z.; Xie, W.; Anderson, E. E.; Miller, T.; Khan, S. A.; Parsons, G. N. Polymer of intrinsic microporosity (PIM) based fibrous mat: combining particle filtration and rapid catalytic hydrolysis of chemical warfare agent simulants into a highly sorptive, breathable, and mechanically robust fiber matrix. *Mater. Today Adv.* **2020**, *8*, 100085.

(48) Wheeler, M. H.; Abramczyk, D.; Puckhaber, L. S.; Naruse, M.; Ebizuka, Y.; Fujii, I.; Szaniszlo, P. J. New Biosynthetic Step in the Melanin Pathway of Wangiella (Exophiala) dermatitidis: Evidence for 2-Acetyl-1,3,6,8-Tetrahydroxynaphthalene as a Novel Precursor. *Eukaryotic Cell* **2008**, *7* (10), 1699−1711.

(49) Geis, P. A.; Wheeler, M. H.; Szaniszlo, P. J. Pentaketide Metabolites of Melanin Synthesis in the Dematiaceous Fungus Wangiella-Dermatitidis. *Arch. Microbiol.* **1984**, *137* (4), 324−328.

(50) Wang, Z.; Tschirhart, T.; Schultzhaus, Z.; Kelly, E. E.; Chen, A.; Oh, E.; Nag, O.; Glaser, E. R.; Kim, E.; Lloyd, P. F.; Charles, P. T.; Li, W.; Leary, D.; Compton, J.; Phillips, D. A.; Dhinojwala, A.; Payne, G. F.; Vora, G. J. Melanin Produced by the Fast-Growing Marine Bacterium Vibrio natriegens through Heterologous Biosynthesis: Characterization and Application. *Appl. Environ. Microbiol.* **2020**, *86* (5), 1−18.

(51) Eisenman, H. C.; Nosanchuk, J. D.; Webber, J. B. W.; Emerson, R. J.; Camesano, T. A.; Casadevall, A. Microstructure of cell wall-associated melanin in the human pathogenic fungus cryptococcus neoformans. *Biochemistry* **2005**, *44* (10), 3683−3693.

(52) Vikrant, K.; Kumar, V.; Kim, K. H.; Kukkar, D. Metal-organic frameworks (MOFs): potential and challenges for capture and abatement of ammonia. *J. Mater. Chem. A* **2017**, *5* (44), 22877−22896.

(53) DeCoste, J. B.; Peterson, G. W. Metal-Organic Frameworks for Air Purification of Toxic Chemicals. *Chem. Rev.* **2014**, *114* (11), 5695−5727.

(54) Yang, Y. J.; Faheem, M.; Wang, L. L.; Meng, Q. H.; Sha, H. Y.; Yang, N.; Yuan, Y.; Zhu, G. S. Surface Pore Engineering of Covalent Organic Frameworks for Ammonia Capture through Synergistic Multivariate and Open Metal Site Approaches. *ACS Cent. Sci.* **2018**, *4* (6), 748−754.

(55) Romero, V.; Fernandes, S. P. S.; Rodriguez-Lorenzo, L.; Kolen'ko, Y. V.; Espina, B.; Salonen, L. M. Recyclable magnetic covalent organic framework for the extraction of marine biotoxins. *Nanoscale* **2019**, *11* (13), 6072−6079.

(56) Kanehashi, S.; Chen, G. Q.; Scholes, C. A.; Ozcelik, B.; Hua, C.; Ciddor, L.; Southon, P. D.; D'Alessandro, D. M.; Kentish, S. E. Enhancing gas permeability in mixed matrix membranes through tuning the nanoparticle properties. *J. Membr. Sci.* **2015**, *482*, 49−55.

(57) Sabetghadam, A.; Liu, X. L.; Benzaqui, M.; Gkaniatsou, E.; Orsi, A.; Lozinska, M. M.; Sicard, C.; Johnson, T.; Steunou, N.; Wright, P. A.; Serre, C.; Gascon, J.; Kapteijn, F. Influence of Filler Pore Structure and Polymer on the Performance of MOF-Based Mixed-Matrix Membranes for $CO_2$ Capture. *Chem. - Eur. J.* **2018**, *24* (31), 7949−7956.

(58) Ilavsky, J.; Jemian, P. R. Irena: tool suite for modeling and analysis of small-angle scattering. *J. Appl. Crystallogr.* **2009**, *42*, 347−353.

(59) D'Onofrio, T. G. Development of a Contact Permeation Test Fixture and Method; ECBC-TR-1141; U.S. Army Research, Development and Engineering Command, 2013.

(60) Kar, F.; Fan, J. T.; Yu, W. Comparison of different test methods for the measurement of fabric or garment moisture transfer properties. *Meas. Sci. Technol.* **2007**, *18* (7), 2033−2038.

(61) Pushpadass, H. A.; Marx, D. B.; Hanna, M. A. Effects of Extrusion Temperature and Plasticizers on the Physical and Functional Properties of Starch Films. *Starch-Starke* **2008**, *60* (10), 527−538.